

Simulations of pre-supernova feedback in spherical clouds

M. Kouniotis^{1*}, R. Wunsch¹, S. Martínez-González², J. Palouš¹, G. Tenorio-Tagle², and S. Ehlerová¹

¹*Astronomical Institute, Czech Academy of Sciences, Bocni II 1401, 141 31 Prague, Czech Republic*

²*Instituto Nacional de Astrofísica, Óptica y Electrónica, AP 51, 72000 Puebla, México*

Accepted XXX. Received YYY; in original form ZZZ

ABSTRACT

We present a one-dimensional radiation-hydrodynamic model of a spherically symmetric cloud evolving under the influence of the self-gravity and the feedback from a star cluster forming in its centre. On one hand, the model is simple due to its 1D geometry, on the other hand, the feedback includes the ionising radiation, stellar winds and the radiation pressure acting on gas and dust. The star cluster is formed from the gas flowing into the cloud centre and the feedback parameters are determined from stellar evolution models and the cluster star forming history. The model is compared to the semi-analytic code `WARPFIELD` implementing similar physical processes and exploring the scenario that the young cluster R136 in the Large Magellanic Cloud was formed due to re-collapse of the shell formed by the previous generation star cluster. A good qualitative agreement is found, however, 3 – 4 times higher stellar mass is needed to disrupt the cloud in our model, because it takes into account (contrary to `WARPFIELD`) self-gravity of the cloud surrounding the shell. We use the model to explore star formation in clouds with different mass, radius and density profile measuring their star formation efficiency (SFE), i.e. the fraction of the cloud mass converted to stars. We found that SFE is a function of a single parameter, $\log(\text{SFE}) \propto -n_{\text{hm}}^{-0.46}$, with n_{hm} being the cloud mean particle density within its half-mass radius. Furthermore, we found that the feedback efficiency, i.e. a fraction of the feedback energy retained by gas, has a nearly constant value $\sim 10^{-3}$.

Key words: hydrodynamics – stars: formation – stars: winds, outflows – ISM: clouds – H II regions

1 INTRODUCTION

The cold gas assembled in the giant molecular clouds (GMC) serves as the building block of stars and star clusters. The efficiency with which the gas converts into stars, however, is long known to be limited based on the large depletion times that well exceed the dynamical ones (Scoville & Hersch 1979; Bigiel et al. 2008; Evans et al. 2009; Kreckel et al. 2018). When normalized to the free-fall time of the cloud, the star formation efficiency (SFE) has been observed to be as low as 0.3% (Utomo et al. 2018; Leroy et al. 2017), with theoretical predictions showing it can reach up to 10% (Semenov et al. 2016; Kim et al. 2021). The observed SFEs essentially reflect the dynamical conditions that regulate the global properties of GMCs in a diversity of environments. On the other hand, the simulated SFEs are largely dependent on the inclusion and the prescription of mechanisms that not only support clouds from gravitational collapse, but can effectively evacuate the sites of star formation.

Theoretical studies that rely solely on the dynamical state of the clouds (with the inclusion of magnetic fields) for regulating star formation, report values of SFE per free-fall time that are well above the observed ones (Padoan & Nordlund 2011; Lee et al. 2015). The magneto-hydrodynamic simulations of turbulent clouds by Grudić et al. (2019) predicted an almost 100% SFE, which however, was substantially reduced to only a few percent when stellar feedback was included. In the same vein, Hopkins et al. (2011) applied a stellar feedback model in high-resolution disc galaxy

simulations and they were able to reproduce the observed Kennicutt–Schmidt relation over a wide range of surface densities –the exclusion of feedback resulted in excessive, by orders of magnitude, star formation rates. Dobbs & Pringle (2013) suggested that cloud dispersion is achieved by the synergistic action of feedback and dynamics of the environment, each contributing differently at the different scales and galactic radii. This combination is also believed to regulate the cloud morphologies, velocity dispersions, and virial parameters, such that the latter do not drive the star formation in GMCs but rather, they are dependent on it (Dobbs et al. 2011; Girichidis et al. 2012; Colín et al. 2013).

The stellar feedback appears to be the key factor for regulating star formation in GMCs by clearing the leftover gas from newborn star clusters. This is well demonstrated by the spatial small-scale (<100 pc) decorrelation between tracers of molecular gas and of star formation (Onodera et al. 2010; Kreckel et al. 2018; Kruijssen et al. 2019b; Semenov et al. 2021). The duration of the phase during which the clusters are embedded within the parent cloud spans only a few Myr (e.g. Hollyhead et al. 2015; Corbelli et al. 2017; Hannon et al. 2019), suggesting clearance of the gas by mechanisms preceding the first supernova (SN) explosions (Kim et al. 2021; Chevance et al. 2020, 2022). Ultimately, most clusters are observed to dissociate from their parent clouds in less than 10 Myr (Grasha et al. 2018, 2019; Turner et al. 2022).

The efficiency of the separate feedback forces, namely the photoionization, the ram pressure from the stellar winds, the direct or reprocessed radiation pressure acting on gas and dust, and the mechanical energy deposited by SNe, has been subject of inves-

* E-mail: kouniotis@asu.cas.cz

tigation by both analytical studies and hydrodynamic simulations. Long considered to be important for the growth of H II regions is the photoevaporation driven by the thermal pressure of the ionized gas (Tenorio-Tagle 1979; Whitworth 1979; Bertoldi & McKee 1990; Matzner 2002). It drives the mass loss in clouds with low surface density (Kim et al. 2018), yet leaving bound massive clouds ($> 10^5 M_\odot$) dynamically unaffected (Dale et al. 2012). The compressed swept-up gas leads to the formation of dense structures that trigger star formation, though only for the short while (Walch et al. 2012; Bending et al. 2020). The effect of radiation pressure was studied by Krumholz & Matzner (2009), who concluded that it is particularly important for the expansion of H II regions surrounding high-mass clusters. More recently, it has been pointed that radiation pressure can dominate the thermal pressure of the warm gas only locally and soon after star formation (Barnes et al. 2020; Ali 2021). When compared to the ram pressure exerted by the shocked winds, the opportunity of radiation pressure to drive the shell dynamics is again confined at the early phases (Gupta et al. 2016), and in cases when the ambient medium is rather dense (Silich & Tenorio-Tagle 2013; Martínez-González et al. 2014). Observations also favor the dominance of photoionization and winds in shaping the morphology of H II regions (e.g. Pellegrini et al. 2011; McLeod et al. 2019). At later evolutionary phases, the contribution from SNe is believed to be less potent in clearing the star-forming gas, as most, if not all of the mechanical energy injected, is shown to escape into the wider environment through low-density channels, which have been carved by the early feedback forces (Rogers & Pittard 2013; Rey-Raposo et al. 2017; Lucas et al. 2020). Nevertheless, SNe are believed to indirectly impact star formation dynamics by establishing and maintaining large-scale turbulence in the cloud (e.g. Padoan et al. 2016).

When the gravitational potential of the cloud is strong enough, or when feedback diminishes and becomes unable to drive the shell expansion e.g. due to leakage of energy, successive star formation episodes are possible to occur following re-collapse of the gas in the centre (e.g. Rugel et al. 2019). Based on this scenario, Rahner et al. (2018, hereafter R18) utilized their analytical one-dimensional code `WARFIELD`, which describes the expansion of H II shells (Rahner et al. 2017), in order to explore the parameters that allowed the formation of the young cluster R136 in the Large Magellanic Cloud (LMC). The bound cluster is located in the star-forming region of 30 Doradus and is embedded within the older and dispersed population NGC 2070, consistent with a scenario in which star formation propagated inwards (Selman et al. 1999; De Marchi et al. 2011). The age separation between the two distinct populations is estimated to exceed 1 Myr (Massey & Hunter 1998; Selman et al. 1999; Sabbi et al. 2012). This offset in time allowed R18 to propose a low threshold for the cloud density, $\sim 500 \text{ cm}^{-3}$, that could have led to re-collapse of the gas due to inefficient feedback from NGC 2070. The assumption by R18 that the natal cloud is in virial equilibrium, however, sets an important limitation to the model because it overrates the strength of the stellar feedback.

Thus stellar feedback acts to disrupt the host molecular cloud, while also regulates its re-collapse. This dual role is the motivation for the current study. We present the results from one-dimensional radiation-hydrodynamic simulations for describing the interplay between the pre-SN feedback forces and the self-gravity of a cold gas cloud. By neglecting here any turbulent forces or external dynamics that would support the cloud against its collapse, we focus on the stellar feedback as the dominant mechanism to regulate the SFE. The objective of the study is twofold. First, we compare the predictions by R18 on the expansion of H II shells with those for a self-gravitating cloud, and refine the parameters that may have enabled R136 to

be formed upon re-collapse of the gas. Second, we proceed to self-consistently infer the SFE, by allowing stars to be formed dynamically in the centre of the cloud until the feedback is able to clear the remaining gas. We explore density models that follow a Schuster profile to enable growth of the central cluster throughout different levels of the cloud compactness. The paper is structured as follows: in Section 2, we describe the physical model of the self-gravitating cloud, the individual feedback processes, and the adopted simulations setups. In Section 3, we introduce the numerical code that implements the physical processes. We present the results of the different setups in Section 4, and draw a link between the gas density and SFE. The limitations following our presented model are discussed in Section 5. The conclusions of the study are given in Section 6.

2 PHYSICAL MODEL

The physical model used in this work consists of a spherically symmetric cloud and a star cluster in its centre providing feedback in the form of radiation and stellar winds. The star cluster can either be inserted into the model initially (setup A), or it can be formed during the calculation from the gas flowing into the central region (setup B).

2.1 Gaseous cloud

We consider a spherically symmetric gaseous cloud with initial density ρ given by a generalized Schuster profile (Ninkovic 1998)

$$\rho(r) = M_{\text{cld}} f_{\text{Sch}}(r, \beta, R_c, R_{\text{cld}}), \quad (1)$$

$$f_{\text{Sch}}(r, \beta, R_c, R_{\text{cld}}) = \frac{C_{\text{Sch}}(\beta, R_c, R_{\text{cld}})}{[1 + (r/R_c)^2]^\beta} \quad \text{for } r \leq R_{\text{cld}} \quad (2)$$

$$C_{\text{Sch}}(\beta, R_c, R_{\text{cld}}) = \frac{3}{4\pi} R_{\text{cld}}^{-3} \left[{}_2F_1 \left(\frac{3}{2}, \beta, \frac{5}{2}, -\frac{R_{\text{cld}}^2}{R_c^2} \right) \right]^{-1} \quad (3)$$

where r is the radial coordinate, β is an index indicating the steepness of the profile, R_c is the core radius, R_{cld} is the outer radius of the cloud, and ${}_2F_1$ is the hypergeometric function. The normalisation function $C_{\text{Sch}}(\beta, R_c, R_{\text{cld}})$ is obtained by integrating the Schuster profile over the sphere. Fig. 1 displays the initial density profile of a cloud with mass $M_{\text{cld}} = 10^{5.5} M_\odot$, radius $R_{\text{cld}} = 30 \text{ pc}$, and several values of β . The initial temperature of the cloud is $T_{\text{cld}} = 10 \text{ K}$, the gas metallicity, Z , is either solar or 0.4 of the solar to match that of the LMC, and the mean molecular weight of the gas particles is $\mu_m = 2.5$ for $Z = Z_\odot$ or $\mu_m = 2.48$ for $Z = 0.4Z_\odot$.

For $r > R_{\text{cld}}$, the cloud is surrounded by low-density ambient gas with temperature $T_{\text{amb}} = 10^4 \text{ K}$ and such a density that establishes a pressure equilibrium across the cloud surface at R_{cld} . This ambient medium is considered for purely numerical reasons (to avoid vacuum in hydrodynamic simulations) and it has no impact on results.

2.2 Star cluster

The star cluster is always located in the centre of the cloud, i.e. the centre of the coordinate system. Its mass is denoted M_* and it can vary with time. The stellar density is given by the Schuster distribution $f_{\text{Sch}}(r, \beta_*, R_{c,*}, R_*)$ of the same form but with different parameters than the density of the cloud (see Eq. 2). For all models we set the slope of the stellar density distribution as $\beta_* = 1.5$, as it approximates well the King density profile of star clusters (King 1962). We set the

Table 1. Parameters of the performed simulations. The first, second and third sections from the top describe parameters of the cloud, star cluster and the computational domain, respectively.

Parameter	Setup A	Setup B
$\log(M_{\text{cld}} [M_{\odot}])$	5.5, 6.0, 6.5	4.5, 5.0, 5.5, 6.0, 6.5
$n_0 [\text{cm}^{-3}]$	500, 700, 1000, 1600, 2500	r -dependent
β	0.0	0.6, 0.8, 1.0, 1.2, 1.4, 1.6, 1.8, 2.0
$R_{\text{cld}} [\text{pc}]$	$[3M_{\text{cld}}/(4\pi n_0 \mu_{\text{m}} m_{\text{H}})]^{1/3}$	10, 20, 30, 40
$R_{\text{c}} [\text{pc}]$	–	1.5
Z	$Z_{\odot}, 0.4Z_{\odot}$	$0.4Z_{\odot}$
SFE ₀	0.01, 0.03, 0.05, 0.10, 0.20, 0.30	0
β_*	1.5	1.5
R_* [pc]	1	0.15
$R_{\text{c},*}$ [pc]	0.2	0.03
comp. domain radius [pc]	30	$R_{\text{cld}} + 10$
number of grid cells	1024	1024 or 2048

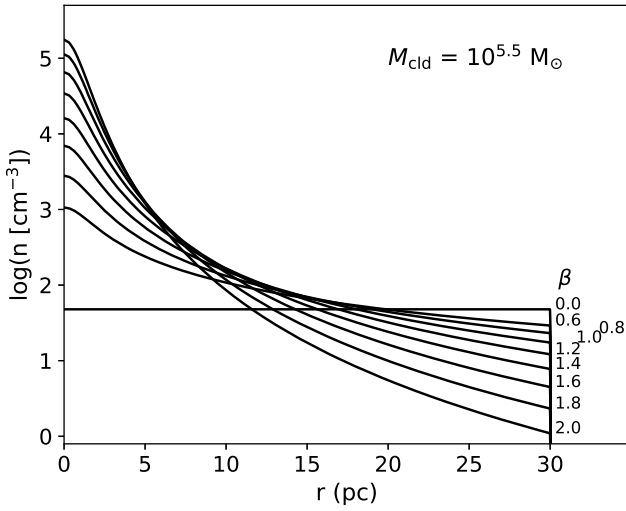


Figure 1. Radial profiles of a cloud with $M_{\text{cld}} = 10^{5.5} M_{\odot}$ and $R_{\text{cld}} = 30$ pc, for the various values of β .

ratio between the star cluster radius and its core radius as $R_* = 5R_{\text{c},*}$, motivated by the observations of the Arches cluster (Espinoza et al. 2009).

The star cluster can be either formed instantaneously in the beginning (we denote this option setup A), or during the calculation from the gas entering the central region (setup B). In the former case, the star cluster mass, $M_* \equiv m_{*,0}$, is a free parameter. The main aim of setup A is to compare the results to the semi-analytic study of a similar model by R18. They parameterize their models by the initial star formation efficiency defined as the ratio between the mass of the star cluster and the cloud, and hence we define the same quantity here as

$$\text{SFE}_0 = m_{*,0}/M_{\text{cld}}. \quad (4)$$

In both setup A and B we use small letters (e.g. $m_{*,0}$) to denote properties of individual stellar populations of the cluster, differing by their age and mass. In setup B, no stars exist in the beginning of the calculation. Instead, all the gas within a sphere with radius R_*

with density higher than $\rho_{\text{w},\text{c}}^1$ is converted into stars at each time step of the hydrodynamic code (see §3). Simultaneously, the mass of the formed stars and the time of their formation are recorded. The density threshold, $\rho_{\text{w},\text{c}}$, is the central (i.e. maximum) density of the star cluster wind resulting from all winds of the stars formed so far (see below for its calculation). This ensures that the star cluster wind is not affected the star formation procedure. Since $\rho_{\text{w},\text{c}}$ is always much lower than the density of the molecular gas (parts of the cloud) inflowing into the star cluster volume due to the gravity, we can consider that basically all the gas that gets into the central region is converted into stars.

The star cluster consists of a set of stellar populations characterised by their mass, $m_{*,j}$, and formation time, t_j , with j being an index of a population. In setup A, there is only a single population with mass $m_{*,0}$. Alternatively, if the cluster is formed continuously (setup B), there is one stellar population per each time step of the hydrodynamic code, and the star cluster mass at time t_j is

$$M_{*,j} = \sum_{k=0}^j m_{*,k} \quad (5)$$

where $m_{*,k}$ is the stellar mass formed between times t_k and t_{k+1} , i.e. during time step k .

We assume that each stellar population is formed at a given time with the initial mass function (IMF) given by Maschberger (2013), which is mathematically convenient approximation of the standard IMF by Chabrier (2003). Stars are formed with masses in range between $0.08 M_{\odot}$ and the minimum between M_* and the upper limit of the stellar evolution tracks $500 M_{\odot}$. Only stars with masses in excess of $9 M_{\odot}$ contribute to the feedback. The feedback parameters are calculated by the simple population synthesis code SYNSTARS using the Bonn Optimized Stellar Tracks (BoOST; Szécsi et al. 2022). The metallicity of the stars is always the same as the metallicity of the cloud, Z , i.e. either Z_{\odot} or $0.4Z_{\odot}$. The calculated feedback parameters of a single population are the stellar wind mechanical luminosity, l_{w} , the mass loss rate, \dot{m}_{w} , the bolometric luminosity, l_{bol} , and the rate of emitted ionising photons per second, q_{i} . Fig. 2 shows the time evolution of these quantities normalized by the mass of the stellar population. Additionally, we calculate from l_{w} and \dot{m}_{w} the central density of the cluster wind, $\rho_{\text{w},\text{c},\text{sp}}$, resulting from stars of a single

¹ Prior to the time when feedback is initiated ($M_* = 100 M_{\odot}$; see §2.3) this density threshold is set to $10^{-29} \text{ g cm}^{-3}$.

population using the semi-analytic code `WINDCALC` (Wünsch et al. 2017) based on the procedure suggested by Silich et al. (2004).

The collective values of the above quantities for the whole cluster can be obtained by summing up over the populations. If we denote by x_j one of the quantities $l_w, \dot{m}_w, l_{\text{bol}}, q_i$ and $\rho_{w,c,\text{sp}}$ at time t_j , the corresponding quantity X_j (i.e. $L_w, \dot{M}_w, L_{\text{bol}}, Q_i$ or $\rho_{w,c}$) for the whole star cluster is

$$X_j = \sum_{k=0}^j x_{j-k} \times m_{*,k} \quad (6)$$

where $x_{j-k} \equiv x(t_j - t_k)$, is the single population quantity with age $t_j - t_k$, normalized per unit stellar mass.

2.3 Stellar feedback

Stars of the central cluster provide feedback via their winds, ionising and non-ionising radiation. The stellar winds feedback is mechanical and it is modelled by inserting the gas and the thermal energy into the cluster volume. The ionising radiation ionises and heats the gas within the Strömgren radius and both types of radiation generate pressure acting on gas and dust which we assume to be dynamically coupled. All forms of the feedback are activated only if $M_* > M_{\text{SF}} \equiv 100 M_\odot$; the time when it happens is called t_{SF} . Threshold M_{SF} approximately corresponds to the mass of the star cluster containing a single massive star considering the standard IMF.

We follow the model by Chevalier & Clegg (1985) assuming that individual stellar winds collide and their kinetic energy is thermalized. As a result, the wind material is heated to $10^7 - 10^8$ K and the high pressure of this hot gas drives the star cluster wind expanding outwards. It can be simulated (see e.g. Cantó et al. 2000; Tenorio-Tagle et al. 2007) by inserting the gas and the thermal energy into the star cluster volume, with insertion densities q_m and q_e , respectively, following the stellar density radial profile,

$$q_m(r) = \dot{M}_w f_{\text{Sch}}(r, \beta_*, R_{c,*}, R_*) \quad (7)$$

$$q_e(r) = L_w f_{\text{Sch}}(r, \beta_*, R_{c,*}, R_*) \quad (8)$$

Stars of the cluster produce radiation with bolometric luminosity $L_{\text{bol}} = L_n + L_i$, where L_n and L_i are luminosities of the non-ionizing ($h\nu < 13.6$ eV) and ionizing ($h\nu > 13.6$ eV) radiation, respectively. The mean energy of the ionizing photons is defined as $\langle h\nu \rangle_i = L_i / Q_i$, where Q_i is the rate of emitted ionising photons per second.

Based on the study of Draine (2011) on dusty H II regions, the radiation pressure force, dF_{rad} , exerted on an infinitesimally thin spherical shell of radius r with volume $dV = 4\pi r^2 dr$ and number density n is given by

$$dF_{\text{rad}} = \frac{L_n e^{-\tau} + L_i \phi}{c} n \sigma_d dr + \alpha_B n^2 \frac{\langle h\nu \rangle_i}{c} dV \quad (9)$$

where $\alpha_B = 2.6 \times 10^{-13} \text{ cm}^3 \text{ s}^{-1}$ is the recombination coefficient to the excited states and σ_d is the dust cross-section per hydrogen nuclei; it is set to $\sigma_d = 1.5 \times 10^{-21} \text{ cm}^2$ for $Z = Z_\odot$ and to $\sigma_d = 6 \times 10^{-22} \text{ cm}^2$ for $Z = 0.4Z_\odot$ (Rahner et al. 2017). We assume that the photons produced by recombinations to the ground state are re-absorbed close to their source (“on-the-spot” approximation; Osterbrock 1974). The functions $\tau(r)$ and $\phi(r)$ for the optical depth and the attenuation of the ionizing radiation, respectively, are given by

$$\frac{d\phi}{dr} = -\frac{1}{Q_i} \alpha_B n^2 4\pi r^2 - n \sigma_d \phi \quad (10)$$

$$\frac{d\tau}{dr} = n \sigma_d \quad (11)$$

Equations (10) – (11) are integrated at each time step of the hydrodynamic code with the boundary conditions $\phi(0) = 1$ and $\tau(0) = 0$, and functions $\phi(r)$ and $\tau(r)$ are determined. The radius at which $\phi(r)$ drops to zero is identified, denoting the radius of the ionization front, R_{IF} .

Equation (9) is then used to calculate the amount of momentum deposited into each grid cell at each time step. Its first right-hand-side (rhs) term represents the radiation pressure of both ionising and non-ionising radiation acting on the dust. The second rhs term describes the momentum deposited by the ionising radiation to the gas, and it is applied only in cells where $\phi(r) > 0$, i.e. for $r < R_{\text{IF}}$. Additionally, the gas at $r < R_{\text{IF}}$ is ionised, i.e. its mean molecular weight is set to μ_i corresponding to the ionized gas, and heated, i.e. its temperature is set to 10^4 K for gas that is cooler than that. Heating by the non-ionising radiation is neglected. Similarly, the reprocessed infrared radiation from dust grains is also ignored, as it is significant only in dust-enriched environments (Skinner & Ostriker 2015), and in general, is shown to be unable to regulate the star formation processes (Menon et al. 2022).

2.4 Simulation setups

In the first set of simulations (setup A), the cloud is uniform ($\beta = 0$) and the star cluster exists from the beginning. We perform 180 simulations varying the four following parameters (see Table 1): the cloud mass, $M_{\text{cld}} = 10^{5.5}, 10^6$, and $10^{6.5} M_\odot$, the initial cloud particle density, $n_0 = \rho_0 / \mu_m m_H = 500, 700, 1000, 1600$, and 2500 cm^{-3} where m_H is the proton mass, the gas and stars metallicity $Z = 0.4Z_\odot$ and Z_\odot , and the initial star formation efficiency, $\text{SFE}_0 = 0.01, 0.03, 0.05, 0.1, 0.2$, and 0.3 that defines the mass of the star cluster, M_* . The star cluster radius is always $R_* = 1$ pc. The selected parameters follow closely those used in R18 to make the comparison straightforward. The computational domain has radius $R_{\text{cd}} = 30$ pc, and consists of 1024 grid cells.

In setup B, the star cluster is formed during the simulation. Uniform clouds (and clouds with small slopes β) have relatively low gas density in their centres leading to the slow inflow of the gas there. As a result, the star cluster mass grows slowly, and the feedback is unable to stop the collapse until the vast majority of the cloud enters the star cluster volume where it is converted to stars. This is clearly a result of the artificial symmetry of the model and as such it is not astrophysically interesting. Therefore, we focus on density profiles with $\beta = 0.6 - 2.0$, at a step of 0.2 dex. Additionally, we vary the cloud mass, $M_{\text{cld}} = 10^{4.5}, 10^5, 10^{5.5}, 10^6$ and $10^{6.5} M_\odot$, and the cloud radius, $R_{\text{cld}} = 10, 20, 30$ and 40 pc. The cloud core radius is always $R_c = 1.5$ pc. Altogether, we perform 160 simulations under setup B (see Table 1). The star cluster radius is $R_* = 0.15$ pc, chosen to be sufficiently small in order to minimize any contribution to the star formation process by the enclosed gas at $t = 0$. The computational domain has radius $R_{\text{cd}} = R_{\text{cld}} + 10$ pc and it consists of 1024 grid cells for simulations with $R_{\text{cld}} < 30$ pc or of 2048 grid cells, otherwise.

Simulations terminate either when the entire cloud has collapsed into the center ($\text{SFE} = 1$), or when, fraction of the gas has been converted into stars and the size of the H II region has reached that of the computational volume. The latter condition indicates that stellar feedback has driven the shell of the residual swept-up cloud out of the explored domain.

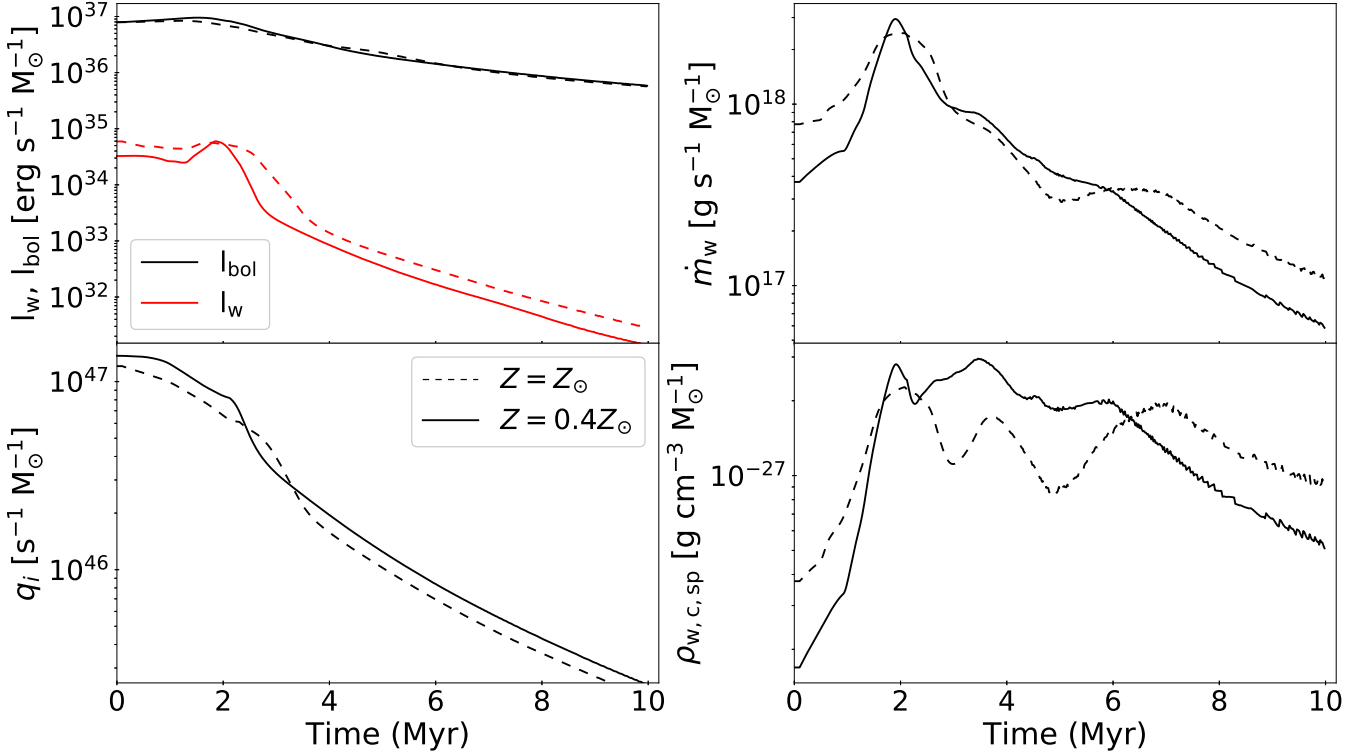


Figure 2. Evolutionary properties per unit stellar mass of a single population as function of time. Calculations were made using the stellar models by Szécsi et al. (2022) at solar metallicity (dashed lines) and at $Z = 0.4Z_{\odot}$ (solid lines).

3 NUMERICAL CODE

To calculate the model evolution, we use a numerical code based on the high-performance parallelized hydrodynamic framework FLASH (Fryxell et al. 2000). We configure FLASH to solve the one-dimensional Euler equations for compressible flow in spherical coordinates in the following form

$$\frac{\partial \rho}{\partial t} + \frac{1}{r^2} \frac{\partial}{\partial r} (r^2 \rho u) = q_m \quad (12)$$

$$\frac{\partial \rho u}{\partial t} + \frac{1}{r^2} \frac{\partial}{\partial r} (r^2 \rho u^2) + \frac{\partial P}{\partial r} = \rho g - q_m u - f_{\text{rad}} \quad (13)$$

$$\frac{\partial \rho E}{\partial t} + \frac{1}{r^2} \frac{\partial}{\partial r} (r^2 (\rho E + P) u) = \rho u g + q_e + q_{\text{rad}} - q_c \quad (14)$$

using the Piecewise Parabolic Method (PPM; Colella & Woodward 1984) with a time step Δt controlled by the Courant–Friedrichs–Levy criterion. In the above equations, t is the time, and ρ , u , and E are the gas density, velocity and the total energy per unit mass, respectively. Quantity E is the sum of the internal energy ε and the kinetic energy per unit mass, i.e.

$$E = \varepsilon + \frac{u^2}{2} \quad (15)$$

where $\varepsilon = P/[\rho(\gamma - 1)]$ with γ being the ratio of specific heats and P being the gas pressure given by the ideal gas equation of state

$$P = \frac{\rho \kappa_B T}{\mu m_H} \quad (16)$$

where κ_B is the Boltzmann constant. The mean molecular weight μ depends on the gas metallicity, Z and temperature, T . For simplicity, we define three values: μ_i for the ionised gas with $T > 9700$ K, μ_a for the atomic gas with $9300 \text{ K} > T > 700$ K, and μ_m for the

molecular gas with $T < 300$ K. Values of μ in transition regions $300 - 700$ K and $9300 - 9700$ K are interpolated linearly. The actual values of μ_i , μ_a and μ_m are calculated from the abundances of species given by Z and the temperature dependent number of free electrons given by Schure et al. (2009, see their Tab. 2). The species abundances are taken from Asplund et al. (2009) for $Z = Z_{\odot}$ and scaled appropriately for other Z values. In this work, we use either the metallicity of the LMC ($Z = 0.4Z_{\odot}$) or the solar metallicity ($Z = Z_{\odot}$). The corresponding mean molecular weights are $\mu_m = 2.48$, $\mu_a = 1.24$, $\mu_i = 0.597$ for $Z = 0.4Z_{\odot}$; and $\mu_m = 2.5$, $\mu_a = 1.25$, $\mu_i = 0.601$ for $Z = Z_{\odot}$.

The star cluster wind is modelled by inserting the mass and energy into the star cluster volume ($r < R_*$) at rate densities q_m and q_e given by Equations 7 and 8, respectively. The momentum in the affected cells is conserved during the insertion procedure (see Wunsch et al. 2008).

The gravitational acceleration, g , consists of two components; one for the self-gravity of the gas, g_{gas} , and one for describing the attractive force between the star cluster, g_* . Both accelerations, at a given coordinate r , are obtained simply from the mass, $M(r)$, enclosed within the sphere of radius r

$$g_{\text{gas}} = -GM_{\text{gas}}(r)r^{-2}, \quad g_* = -GM_*(r)r^{-2} \quad (17)$$

where G is the constant of gravity. For the star cluster, the enclosed mass is

$$M_*(r) = \begin{cases} M_* C_{\text{Sch}}(\beta_*, R_{c,*}, r) & \text{for } r \leq R_* \\ M_* & \text{for } r > R_* \end{cases} \quad (18)$$

The enclosed mass of the gas, $M_{\text{gas}}(r)$, is calculated at each time step by a fast integrator described below.

Determining the gravitational acceleration due to gas self-gravity

and solving radiative transport equations (10) and (11) leads to the same mathematical problem – calculating an integral of a certain power of the particle density, n , from the centre to each grid cell at each time step. For that, we develop a fast parallel integrator calculating quantity y_j for each grid cell j

$$y_j = \sum_{i=0}^j n_i^p \Delta x_i \quad (19)$$

where n_i is the particle density in grid cell i , p is an integer number, and Δx_i is either the radial extent of the i -th grid cell Δr_i or its volume ΔV_i . The integrator utilizes a property of the FLASH domain decomposition algorithm guaranteeing that sub-domains assigned to individual processors are contiguous. This significantly simplifies the communication, as only the sums over the whole sub-domain have to be sent to other processors. The enclosed mass, $M_{\text{gas}}(r)$, is then calculated by setting $p = 1$ and $\Delta x_i = \Delta V_i$; the first rhs term of Eq. 10 by setting $p = 2$ and $\Delta x_i = \Delta V_i$; and the first rhs term of Eq. 11 by setting $p = 1$ and $\Delta x_i = \Delta r_i$. The calculation of the second rhs term of Eq. 10 uses $\Delta x_i = \Delta r_i$, and additionally adopts ϕ_i from the previous hydrodynamic time step.

The gas loses energy by emitting the radiation at rate

$$q_c = -n_{\text{H}}^2 \Lambda(T, Z) \quad (20)$$

where n_{H} is the mean mass per the Hydrogen nuclei and $\Lambda(T, Z)$ is the cooling function by Schure et al. (2009). They tabulate it for each specie individually making it convenient to scale it for any metallicity. The energy losses are assumed to be optically thin, i.e. the energy is subtracted from each grid cell and it is not followed further. To account to the ionising radiation heating, we use a simple approximation of the constant H II region temperature: the temperature in grid cells where $\phi > 0$ (intensity of the ionising radiation is non-zero) is not allowed to drop below 10^4 K. In grid cells where $\phi = 0$, a constant heating is used with rate $q_{\text{rad}} = n_{\text{H}} \Gamma$ with $\Gamma = 2 \times 10^{-26}$ erg s $^{-1}$ taking into account several common heating processes in the interstellar medium (Koyama & Inutsuka 2002).

The acceleration due to the radiation pressure in Eq. 13, $f_{\text{rad}} = dF_{\text{rad}}/dV$, is given by Eq. 9. It can be easily determined for each grid cell knowing functions ϕ and τ .

We investigate the sensitivity of the model evolution on the grid resolution. For our test purposes, we run setup B simulations of five different cloud models using three resolutions (grid cell numbers). The results are provided in the appendix (Fig. A1) and they show that the differences among the calculations at different resolution are smaller than ~ 0.1 dex for all five models.

4 RESULTS

The results of the two simulation sets are reported below. Common features of the model evolution are described in §4.1, followed by §4.2 and §4.3 discussing results of the setup A and setup B runs, respectively.

4.1 General model evolution

The interaction of the star cluster wind and radiation with the cloud leads to the establishment of a bubble described by Castor et al. (1975); Weaver et al. (1977). Fig. 3 shows its structure and evolution for a setup A model with parameters $M_{\text{cl,d}} = 10^{5.5} M_{\odot}$, $n_0 = 1000$ cm $^{-3}$ and $\text{SFE}_0 = 0.03$ (i.e. $M_* \approx 10^4 M_{\odot}$). The components of the bubble are well visible e.g. at 0.4 Myr (see the top

right panel of Fig. 3, and the inset zooming in on the H II region and the cold shell). The wind is formed within the star cluster, and at its edge the wind velocity crosses the sound speed (see cyan and red thin lines, cfn. Chevalier & Clegg 1985). The wind expands freely, up to the reverse shock, $R_{\text{RS}} \approx 2$ pc where its kinetic energy is thermalized and the gas is heated to $\sim 10^8$ K. The shocked wind region extends up to the contact discontinuity at $R_{\text{CD}} \approx 6.4$ pc, where it adjoins to the cloud gas ionised by the stellar radiation (H II region; see the drop of the temperature, green dash-dotted line, from 10^8 to 10^4 K). The H II region is relatively thin as it is compressed by the high pressure of the shocked wind. Its outer edge is at the ionisation front $R_{\text{IF}} \approx 6.6$ pc, where the high energy photons ($h\nu > 13.6$) are depleted. The H II region is surrounded by the thin shell of cold gas composed of the accreted cloud material. The temperature of the shell is close to 10 K, however, its outer edge at the shock front, $R_{\text{SF}} \approx 6.7$ pc, is slightly heated by the compression there. The original cloud is located at even higher radii, falling inwards onto the shell due to the gravity (see the cyan line of the gas velocity in Fig. 3). The outermost part of the computational domain is filled by the rarefied warm ambient medium.

In setup A runs, the cluster is inserted into the simulation in the beginning, and it is always massive enough to form the bubble almost immediately. In setup B runs, it may take a certain time until the cluster mass reaches the value when the feedback is powerful enough to reverse the cloud collapse. We define time t_e when the thermal pressure in the central region exceeds the ram pressure of the infalling cloud and the bubble starts to expand. Furthermore, the inflow of gas into the star cluster volume and the growth of M_* stop at t_e .

Once the bubble is formed, it expands and the dense cold shell on the bubble surface accretes the cloud mass. Simultaneously, the cloud collapses adding more mass to the shell. This process can lead to two outcomes: either the cloud becomes unbound and the expansion continues indefinitely, or the expansion stops at some point and the shell re-collapses into the centre where it is immediately converted into stars. Fig. 3 shows the latter case, with the shell starting to collapse at ~ 0.7 Myr and reaching the centre shortly before 2 Myr. The time evolution of the ionisation front, R_{IF} , can be seen also in Fig. 4 (middle row, right column, yellow solid line).

4.2 Models with pre-existing star cluster (setup A)

In Fig. 4, we display the evolution of the outer radius of the H II region, R_{IF} , for all setup A models. Depending on the initial parameters $M_{\text{cl,d}}$, n_0 and SFE_0 , there are two qualitatively different types of behaviour. With high $M_{\text{cl,d}}$, high n_0 and low SFE_0 , the bubble expands to a certain radius and then re-collapses. In the opposite case, i.e. low $M_{\text{cl,d}}$, low n_0 and high SFE_0 , the bubble expansion continues indefinitely and the cloud is unbound. Considering the extreme cases, in the most massive and compact cloud with $M_{\text{cl,d}} = 10^{6.5} M_{\odot}$ and $n_0 = 2500$ cm $^{-3}$, the bubble re-collapses even with the highest $\text{SFE}_0 = 0.3$ corresponding to the star cluster with mass $M_{*,0} \approx 10^6 M_{\odot}$ (see the top left corner of Fig. 4). On the other hand, the cloud with $M_{\text{cl,d}} = 10^{5.5} M_{\odot}$ and $n_0 = 500$ cm $^{-3}$ is unbound with all models with $\text{SFE}_0 \geq 0.03$ ($M_{*,0} \approx 10^4 M_{\odot}$; bottom right corner of Fig. 4).

Time at which the bubble in bound models re-collapses is given by the cloud free-fall time

$$\tau_{\text{ff}} = \left(\frac{3\pi}{32G\rho_0} \right)^{1/2} \approx 1.03 \left(\frac{n_0}{10^3 \text{ cm}^{-3}} \right)^{-1/2} \text{ Myr} . \quad (21)$$

In models with low SFE_0 , where the impact of the feedback from the

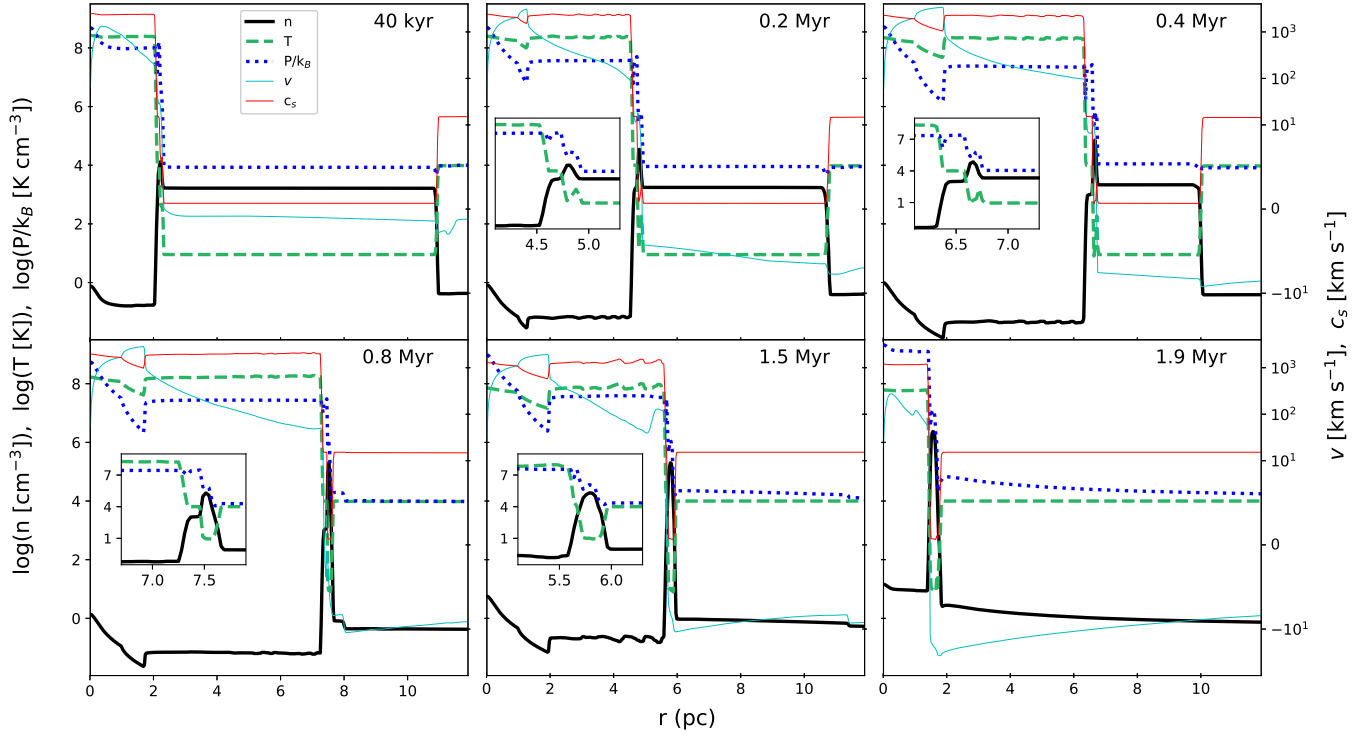


Figure 3. Radial profile at different times of the various properties of the gas; particle density (black thick line), temperature (green dashed line), and pressure (blue dotted line) in log scale (left axis), as well as velocity (cyan thin line) and sound speed (red thin line) in km s^{-1} (right axis). The simulations follow setup A assuming a cloud with $M_{\text{cld}} = 10^{5.5} M_{\odot}$ and $n = 1000 \text{ cm}^{-3}$, which collapses against the feedback from a central cluster that is formed with $\text{SFE}_0 = 0.03$. A zoomed view of the shell is displayed by insets within the panels for $t = 0.2 - 1.5 \text{ Myr}$. For simplicity, only the particle density, temperature and pressure are shown in the insets.

star cluster is not significantly affecting the overall cloud collapse, the bubble collapses at almost exactly τ_{ff} . The bubble re-collapse takes longer for models with higher SFE_0 . In several cases with SFE_0 close to the value needed to unbound the cloud we observe periods when R_{IF} stays almost constant for several Myr due to the equilibrium between the thermal pressure of the bubble interior and the ram pressure of the infalling cloud. This resembles behaviour described in Tenorio-Tagle et al. (2003). We stress, however, that the exclusion of supernova feedback from our model renders the outcome beyond $t \sim 3.5 \text{ Myr}$ uncertain.

To explore the impact of metallicity on the bubble evolution, we calculate all setup A models with two values $Z = Z_* = Z_{\odot}$ and $Z = Z_* = 0.4Z_{\odot}$, shown in Fig. 4 by dashed and solid lines, respectively. On one hand, the mechanical luminosity of stellar winds, L_w , is higher with higher Z_* due to the wind line-driven nature, making the feedback more efficient. On the other hand, the bolometric luminosity of the star cluster is slightly lower with higher Z_* making the radiation pressure feedback less efficient. Additionally, higher gas metallicity, Z , results in higher cooling of the hot gas reducing its temperature and hence the thermal pressure. Fig. 4 shows that the effect of higher L_w dominates in all cases and the bubble expands faster with higher Z and Z_* . Essentially thus, our findings contradict those by studies that suggest low metallicity to be supportive for the growth of H II regions and the reduction of SFE, however ignoring the impact of stellar winds (e.g. Fukushima et al. 2020; Ali 2021).

In Fig. 5, we display time t_{coll} during which the bubble re-collapses as a function of SFE_0 and n_0 , for runs with $Z = 0.4Z_{\odot}$. In the left panel showing the cloud with $M_{\text{cld}} = 10^{6.5} M_{\odot}$, a dashed line indicates the threshold found by R18 to separate models where the

cloud is bound and unbound. Our results are qualitatively similar, however, the threshold (shown by solid line in Fig. 5) is shifted to higher SFE_0 or lower n_0 . To unbound the cloud, either SFE_0 higher by factor of 3–4, or n_0 lower by factor ~ 5 is needed in comparison to R18. The main reason for this difference is that the self-gravity of the cloud is included in our model, however, it is not in the R18 model (we remind that R18 include the self-gravity of the shell, however, the cloud is assumed to be in virial equilibrium, i.e. stabilised against the gravitational force by the turbulent and/or magnetic pressure).

Following R18, we apply the model of the shell re-collapse to explain the origin of NGC 2070 and its younger central star cluster R136. NGC 2070 corresponds to the initial star cluster, and for its mass we adopt range $8.7 \times 10^4 - 4.5 \times 10^5 M_{\odot}$ (Bosch et al. 2009; Cignoni et al. 2015), shown as gray-shaded area in Fig. 5. Another constrain is given by the age difference between NGC 2070 and R136, which is at least 1 Myr. It corresponds to time t_{coll} of the shell re-collapse and it is shown by color in Fig. 5. With cloud mass $10^{6.5} M_{\odot}$, several runs with $\text{SFE}_0 = 0.03 - 0.1$ and $n_0 \lesssim 1000 \text{ cm}^{-3}$ fulfill both constrains and are thus consistent with the observations. Clouds with lower masses need higher SFE_0 and higher n_0 to justify the above discussed scenario.

4.3 Models with continuous star formation (setup B)

In setup B runs, the star cluster is formed during the simulation from the gas that enters the central sphere with radius $R_* = 0.15 \text{ pc}$. Fig. 6 shows time evolution of the star cluster mass, M_* , for a cloud with initial mass and radius $M_{\text{cld}} = 10^5 M_{\odot}$ and $R_{\text{cld}} = 20 \text{ pc}$, respectively, and for different density slopes β . All the runs show the

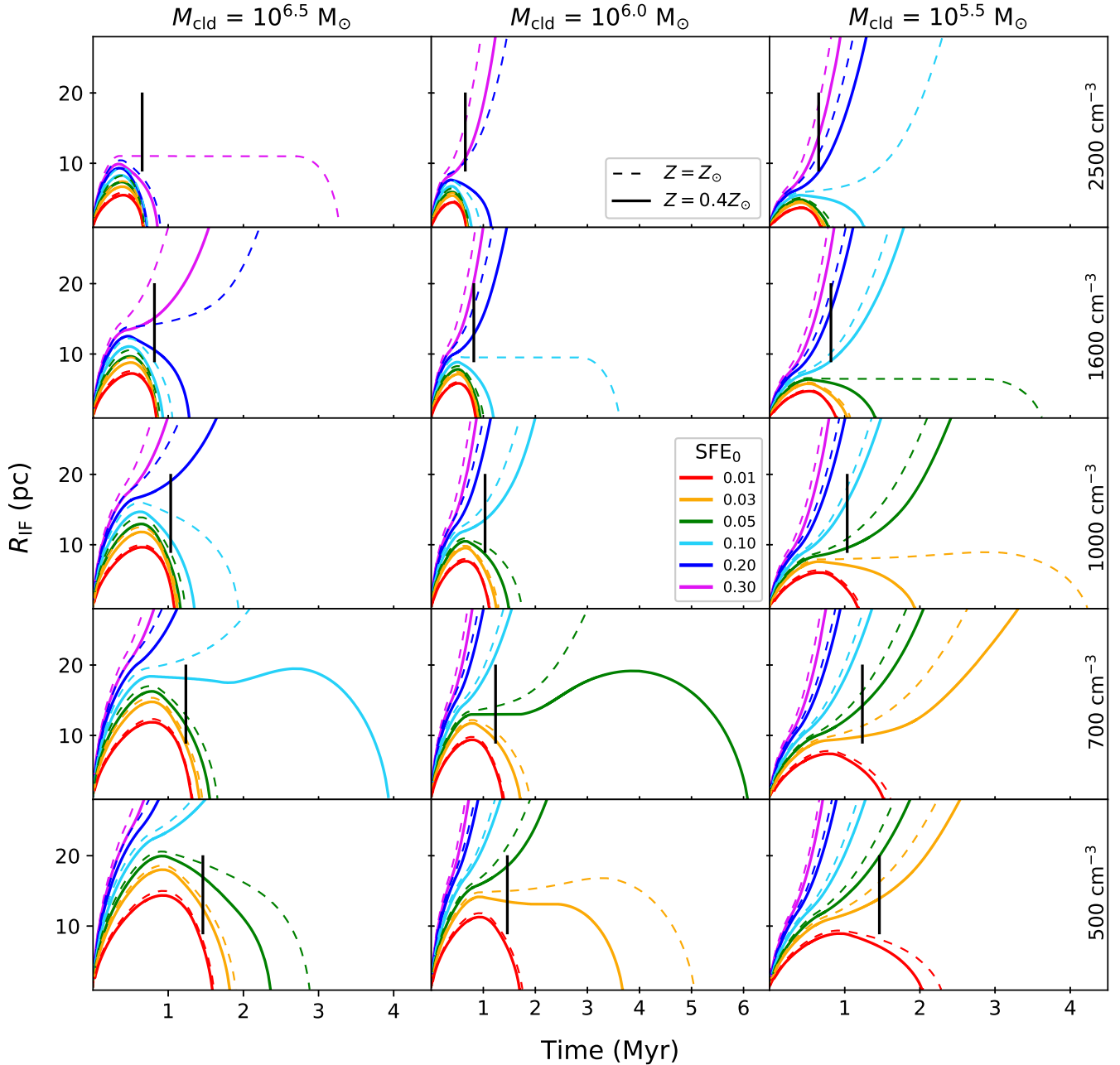


Figure 4. Evolution of the outer radius of the H II region as function of the mass and density of the cloud. The plotted lines are color coded with respect to SFE_0 . Dashed and solid lines show models $Z = Z_\odot$ and $Z = 0.4Z_\odot$, respectively. In each panel, τ_{ff} is indicated by a vertical line.

qualitatively same behaviour. Initially, M_* grows relatively slowly as the cloud starts to contract due to the self-gravity. At a certain time, the mass of the cluster starts to contribute significantly to the gravitational acceleration and the M_* growth rate suddenly increases. Shortly after that, M_* exceeds threshold $100 M_\odot$ and the feedback is switched on. Then, M_* continues to grow with decreasing rate until time t_e (denoted by asterisk in Fig. 6) when the feedback is strong enough to create an expanding bubble and to stop the inflow of the gas into the star cluster volume. Finally, the bubble expands until it reaches the computational domain boundary ending the simulation. All setup B models exhibit only a single period of star formation; once the star cluster mass was stopped at t_e , the feedback was always strong enough to unbound the cloud. That allows us to define the star

formation efficiency, SFE^2 , as the ratio of the star cluster mass (at t_e when it is definitely formed) and the initial cloud mass M_{cld}

$$SFE = M_*(t_e)/M_{cld}. \quad (22)$$

With increasing the steepness of the cloud density profile, β , the M_* grows faster due to the higher rate at which gas flows into the star cluster volume. Additionally, higher β results in the higher density of the gas surrounding the star cluster leading to the suppression of the feedback from more massive star clusters. As a consequence, SFE

² Not to be confused with SFE_0 , which is a free parameter setting the mass of the pre-existing star cluster in setup A models.

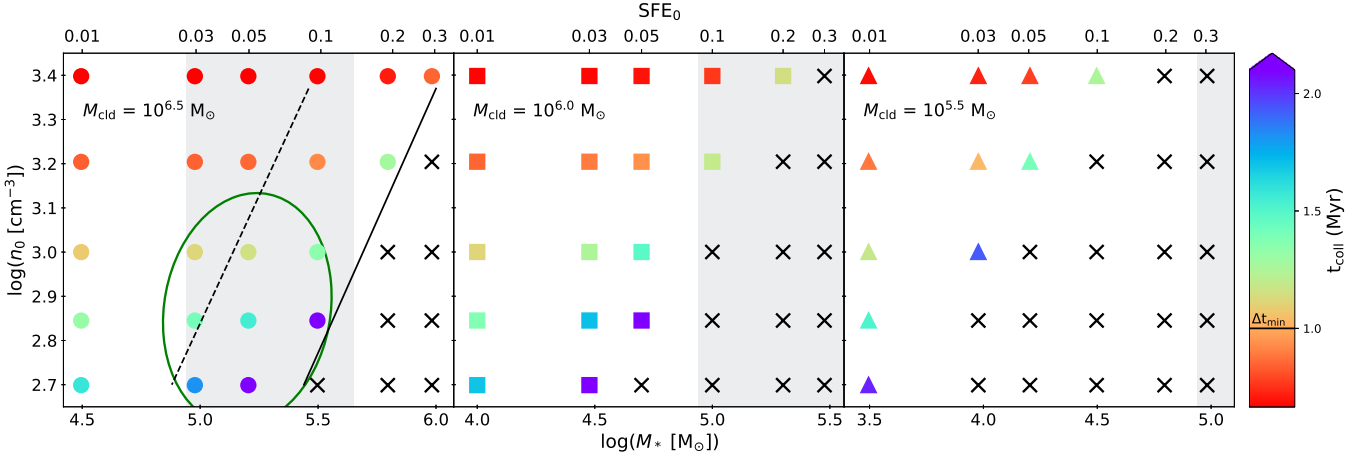


Figure 5. Collapsing times of the shell as function of cloud density and SFE_0 . The “X” markers stand for simulations that predict a shell expansion. For a cloud with $M_{\text{cld}} = 10^{6.5} M_{\odot}$, the dashed line indicates the threshold SFE_0 from [Rahner et al. \(2018\)](#) that differentiates collapsing models from those with a disruptive feedback. Our respective threshold (solid line) is shown to be 3 – 4 times higher. The mass of NGC 2070 as source of feedback at $t = 0$ is displayed with a grey shaded area. An horizontal line in the colorbar indicates the minimum age separation between NGC 2070 and R136, the latter being suggested to have formed upon re-collapse of the gas. For $M_{\text{cld}} = 10^{6.5} M_{\odot}$, the models consistent with the re-collapse scenario are enclosed by a green ellipse.

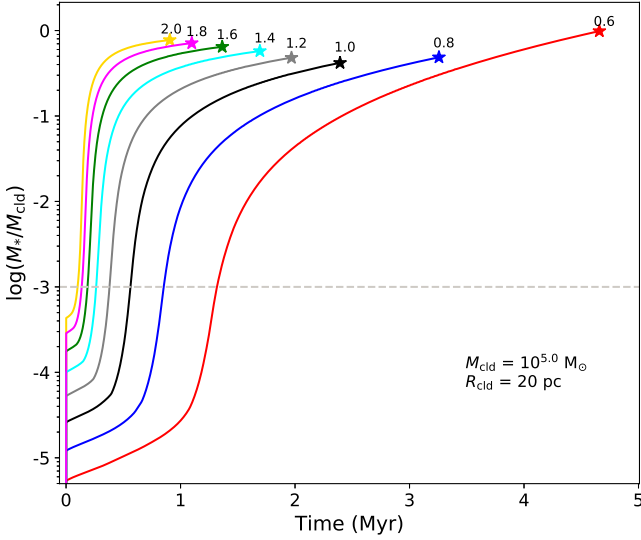


Figure 6. Evolution of the stellar mass relative to the mass of the cloud, for the different profiles of gas density. The mass and radius of the cloud at $t = 0$ are here set as $M_{\text{cld}} = 10^5 M_{\odot}$ and $R_{\text{cld}} = 20$ pc. For each of the models, we indicate the β value of the cloud steepness, and mark the point (asterisk) when the stellar feedback begins to disperse the residual gas. At the latter point, the mass of the cluster defines the SFE of the model. A dashed horizontal line indicates the $100 M_{\odot}$ threshold in the stellar mass for initiating feedback in our simulations. Calculations over the entire set of cloud parameters are shown in the appendix (Fig. B1).

rises with increasing β in the range $\beta = 0.8 - 2.0$. On the other hand, M_* grows slowly in clouds with $\beta < 0.8$, and lower β results in longer time before the feedback is able to create the bubble and in higher fraction of the cloud being converted into stars. In other words, high SFE is reached either with high β due to the fast growth of M_* in the beginning and the high central pressure, or with low β due to the slow M_* growth allowing the cloud collapse to proceed to the advanced stage. Intermediate values of β ($\sim 0.8 - 1.0$) lead to the lowest SFE. We denote β_{min} the slope for which SFE reaches minimum value for

given M_{cld} and R_{cld} ; the corresponding star formation efficiency is $SFE(\beta_{\text{min}})$. The time evolutions of M_* for the entire set of setup B runs are provided in the appendix (Fig. B1).

We search for a single parameter combining M_{cld} , R_{cld} and β giving the tightest relation with SFE, and found that the mean particle density within the cloud half-mass radius works well in this respect. It is defined as

$$n_{\text{hm}} = \frac{3M_{\text{cld}}}{8\pi\mu_c m_{\text{H}} R_{\text{hm}}^3}, \quad (23)$$

where R_{hm} is the numerically determined half-mass radius of the cloud at time t_{SF} when the stellar feedback is activated, i.e. M_* reaches M_{SF} . Fig. 7 shows SFE as a function of n_{hm} for all setup B models. The color and shape of symbols represent the initial cloud density slope β . It can be seen that all the models can be divided into two groups. First, there are models with SFE nearly 100% (i.e. $\log(\text{SFE}) \approx 0$) with typically $\beta < 1$. They are models where it takes a long time until M_* reaches M_{SF} , and when it finally happens, the cloud collapse proceeded so much that the feedback bubble cannot be formed unless the vast majority of the cloud is converted into stars. Second, the majority of models lie along the line given by the relation

$$\log(\text{SFE}) = -5.43 \times \left(\frac{n_{\text{hm}}}{\text{cm}^{-3}} \right)^{-0.46}. \quad (24)$$

We found the second group astrophysically more interesting, because the volume density in real molecular clouds varies significantly more than in our model, and the situation that the feedback bubble cannot be created before the whole cloud collapses (as in the first group) is highly improbable.

Fig. 8 compares the energy of the feedback to the energy retained by the gas, for a model with $M_{\text{cld}} = 10^5 M_{\odot}$, $R_{\text{cld}} = 20$ pc and $\beta = 0.8$. The blue line in the top panel represents the cumulative energy inserted by the all forms of the feedback:

$$E_{\text{ins}}(t) = \int_{t_{\text{SF}}}^t [L_{\text{bol}}(t') + L_{\text{w}}(t')] dt'. \quad (25)$$

The other lines are components of the energy associated with gas at given time, specifically, the internal energy E_{int} (cyan), the kinetic

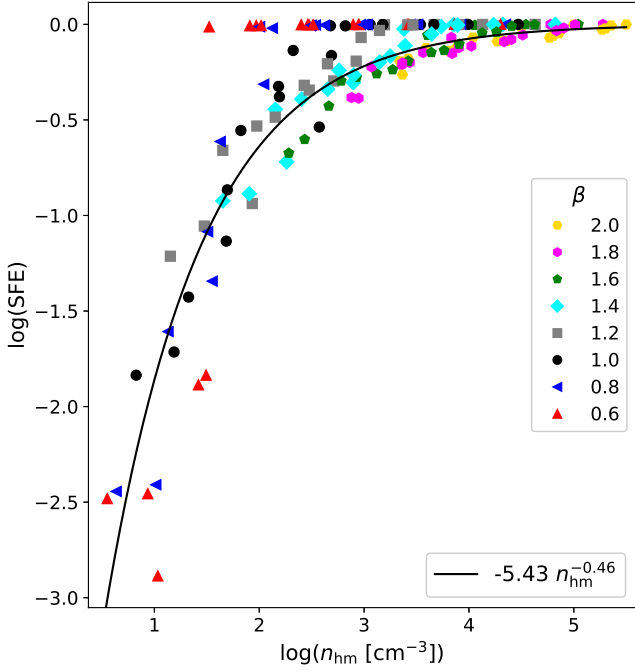


Figure 7. Logarithm of the star formation efficiency (SFE) as a function of the mean particle density within the half-mass radius of the cloud, for the all setup B models. The color of symbols represents β . The best fit to the data (disregarding points with $\beta < 1$ that show $\log(\text{SFE}) \approx 0$) is displayed with a solid black line (Eq. 24).

energy E_{kin} (green), and the gravitational binding energy (magenta)

$$E_{\text{grv}}(t) = -G \int_0^{R_{\text{cd}}} \frac{[M_{\text{cld}}(r, t) + M_*(r, t)]}{r} \rho(r, t) 4\pi r^2 dr \quad (26)$$

where $M_{\text{cld}}(r, t)$ and $M_*(r, t)$ are fractions of the cloud mass and the cluster mass below radius r at time t , respectively, and $\rho(r, t)$ is the gas density. The total energy of the gas is $E_{\text{tot}}(t) = E_{\text{int}}(t) + E_{\text{kin}}(t) + E_{\text{grv}}(t)$.

The energy retained by the gas can be estimated by subtracting the initial total gas energy $E_{\text{tot}}(0)$ from $E_{\text{tot}}(t)$. This allows us to define the instantaneous feedback efficiency

$$\epsilon_f(t) = \frac{E_{\text{tot}}(t) - E_{\text{tot}}(0)}{E_{\text{ins}}(t)}. \quad (27)$$

The bottom panel show the feedback efficiency from the same models as the top panel. Initially, after t_{SF} when the feedback is activated, $\epsilon_f(t)$ stays low ($\sim 10^{-6}$) until the expanding bubble is formed at $t \approx 3.3$ Myr. Then, $\epsilon_f(t)$ quickly grows to almost 3×10^{-4} , and at the end it drops due to the bubble leaving the computational domain. Finally, we define the overall feedback efficiency (or simply the feedback efficiency) ϵ_f as a maximum over the whole time evolution of a given model.

Fig. 9 shows ϵ_f as function of n_{hm} for all setup B models. The color and shape of symbols represent the SFE of a given model. Interestingly, if we disregard models with SFE close to unity, majority of models have ϵ_f within $10^{-3.5} - 10^{-2.5}$. There is a weak trend with n_{hm} , making ϵ_f higher for the high n_{hm} (as well as for the higher SFE) with ϵ_f reaching 10^{-2} for the highest $n_{\text{hm}} \sim 10^4 - 10^5 \text{ cm}^{-3}$. Additionally, models with the lowest $n_{\text{hm}} \lesssim 10 \text{ cm}^{-3}$ seem to have slightly higher values of ϵ_f , too.

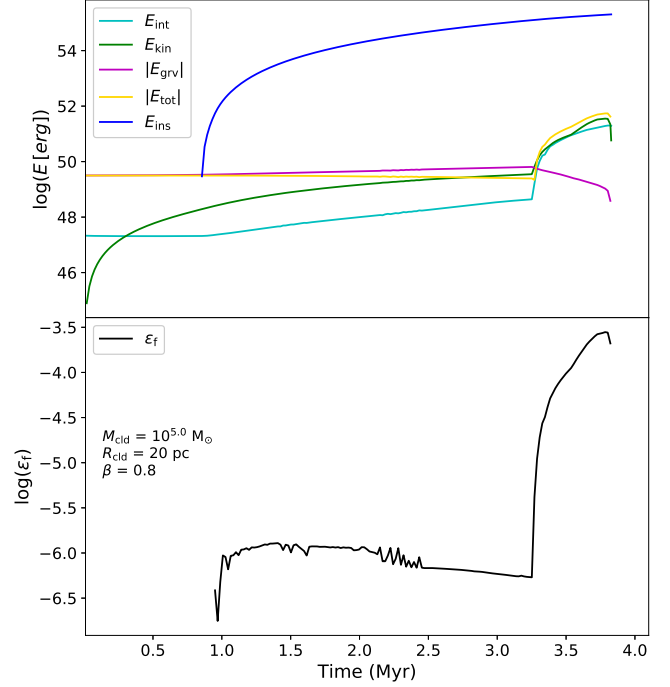


Figure 8. Top: Time evolution of the logarithm of the cumulative energy inserted by the all different forms of feedback, $E_{\text{ins}}(t)$ (Eq. 25, blue line), and logarithms of components of the gas energy: the internal energy $E_{\text{int}}(t)$ (cyan), the kinetic energy $E_{\text{kin}}(t)$ (green), the gravitational energy $E_{\text{grv}}(t)$ (magenta, Eq. 26), and the total energy $E_{\text{tot}}(t)$ (yellow). **Bottom:** Time evolution of the logarithm of the instantaneous feedback efficiency $\epsilon_f(t)$ (see Eq. 27). All lines in both panels represent a model with $M_{\text{cld}} = 10^5 M_{\odot}$, $R_{\text{cld}} = 20 \text{ pc}$, and $\beta = 0.8$.

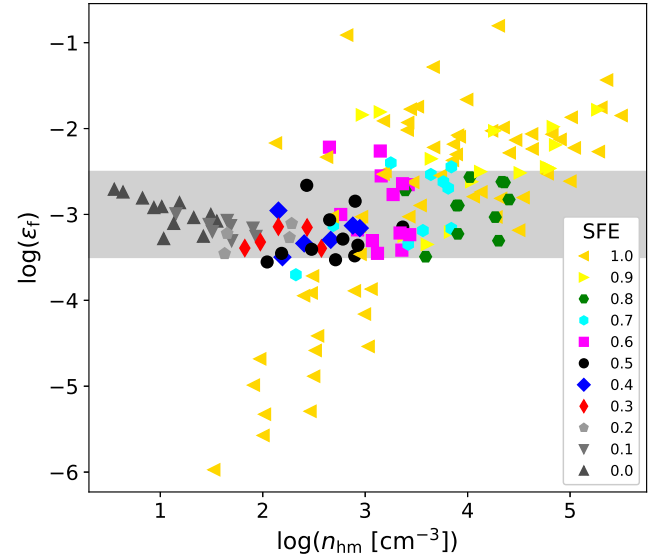


Figure 9. Logarithm of the feedback efficiency ϵ_f as a function of n_{hm} . The shaded area indicates ϵ_f values of $10^{-3.5} - 10^{-2.5}$.

5 DISCUSSION

The presented model includes many limitations making its direct comparison to observations difficult; it should be understood rather as a toy model exhibiting some interesting properties improving our insight into how the feedback regulates star formation. Most of the limitations come from the imposed spherical symmetry. However, this also makes the model simple and hence computationally cheap allowing calculations with many parameter combinations, and relatively easy to interpret. Moreover, the model includes the (probably) three most important forms of pre-SN stellar feedback, i.e. the ionising radiation, stellar winds and the radiation pressure, implemented on a relatively detailed level. The obtained results can also be used as a sub-grid model for simulations of star formation and galaxies on larger scales (e.g. [Walch et al. 2015](#)).

One of the most important processes that cannot be properly modelled in 1D is the turbulence in molecular clouds, and it is known to be an important agent regulating the star formation (e.g. [Elmegreen & Scalo 2004](#); [Mac Low & Klessen 2004](#)). Its impact on the star formation is both positive and negative. On one hand, it provides an additional pressure and it prevents a monolithic collapse. On the other hand, the turbulence can also lead to density enhancements within the cloud, triggering the local collapse ([Klessen et al. 2000](#); [Federrath & Klessen 2012](#)). Numerical simulations collectively predict an anticorrelation between SFE and the virial parameter (α_{vir}), the latter being function of the (initial) turbulent velocity that defines the level of the cloud boundedness ([Clark & Bonnell 2004](#); [Padoan et al. 2012](#); [Bertram et al. 2015](#); [Raskutti et al. 2016](#); [Howard et al. 2016](#); [Kim et al. 2021](#)). From the observational point of view, however, solid conclusions on the negative effect of turbulence on SFE can not be drawn. For example, α_{vir} shows no correlation with SFE in Galactic molecular clouds ([Vutisalchavakul et al. 2016](#)) nor it is linked to the likelihood of clouds in the LMC hosting young stellar objects ([Wong et al. 2011](#)).

More generally, the assumption of spherical symmetry does not allow to include the cloud density structure. It can impact the efficiency of the feedback in dispersing the gas and hence alter the SFE. A highly-structured medium with cavities and low-density channels can allow a significant fraction of photons and momentum to escape reducing thus the coupling of the feedback forces to the gas ([Dale et al. 2014](#); [Rogers & Pittard 2013](#); [Raskutti et al. 2017](#); [Chevance et al. 2022](#)).

In addition, a shell that undergoes fragmentation may trigger star formation in sites other than the centre ([Tenorio-Tagle et al. 2003](#)), thereby altering the SFE of the cloud. Processes that can attenuate the impact from the stellar winds, such as mixing and cooling in the interface between the shocked gas regime and the ionized gas (e.g. [Dunne et al. 2003](#); [Lancaster et al. 2021](#)) should be further taken into consideration.

Finally, the role of the environment in regulating the SFEs should be taken into account, as it governs the systematic differences between GMCs in different galaxies ([Hughes et al. 2013](#)) and at different galactocentric radii ([Shetty et al. 2012](#); [Colombo et al. 2014](#); [Sun et al. 2020](#)). Coupled to the galactic potential and large-scale dynamics such as the shear, GMCs experience changes in their morphological and kinematic state ([Koda et al. 2009](#); [Kruijssen et al. 2019a](#)) that ultimately impact their lifetimes and SFEs ([Jeffreson & Kruijssen 2018](#); [Colombo et al. 2018](#); [Meidt et al. 2020](#)). Other external mechanisms that regulate the cloud-scale properties and star formation include compressive shocks induced by nearby star-forming activity ([Wei et al. 2012](#)) and the cloud-cloud collisions ([Fukui et al. 2021](#); [Dobbs et al. 2011](#)).

6 CONCLUSIONS

We performed 1D radiation-hydrodynamic simulations to describe the interplay between the pre-SN feedback and the self-gravity of a molecular cloud. The feedback includes the ionising radiation, stellar winds and the radiation pressure on gas and dust from ionising and non-ionising radiation. We study two setups addressing different objectives. Setup A runs start with the star cluster existing from the beginning, with a fixed mass given by parameter SFE_0 and the cloud has always uniform density. The aim is to revisit the semi-analytic work by R18 with a model including the cloud self-gravity and dynamics. In setup B runs, the star cluster forms from the gas entering the central region, and this allows to study SFE as a function of the model parameters. The cloud density is higher in the centre with various slopes, because a uniform cloud stays uniform during the collapse and does not result in astrophysically meaningful results (leads always to $\text{SFE} = 1$). Our results are synopsized as follows.

(i) Comparison to R18 studying a similar model shows that a star cluster with 3 – 4 times higher mass is needed to disrupt the uniform cloud by the feedback. Alternatively formulated, for the same star cluster, the cloud needs to have ~ 5 times lower density to get disrupted in our model than in R18. This difference is almost entirely due to the self-gravity causing the collapse of the cloud not overrun yet by the shell, which is included in our model while it is not in R18.

(ii) Calculations with higher metallicity exhibit more efficient feedback. In our setup A runs with solar metallicity, the feedback bubble expands slightly faster and the cloud disruption is easier than in runs with LMC metallicity ($0.4Z_{\odot}$). It is due to the higher mechanical luminosity of stellar winds of stars with higher metallicity.

(iii) Our model is qualitatively consistent with the suggestion of R18 that the R136 star cluster in NGC 2070 might have been formed by the re-collapse of the shell. Assuming the mass of the 30 Doradus natal cloud $M_{\text{clid}} = 10^{6.5} M_{\odot}$, the re-collapse scenario may take place with cloud density $n_0 \lesssim 1000 \text{ cm}^{-3}$.

(iv) The star formation efficiency is a function of a single parameter combining the all properties of the cloud in our model. This parameter is the mean density within the cloud half-mass radius, n_{hm} , and it is given by the cloud mass, radius and the slope of its density profile. The star formation efficiency in our setup B runs, i.e. the mass of the formed star cluster normalized by the initial mass of the cloud, follows approximately the relation $\log(\text{SFE}) = -5.43(n_{\text{hm}}/\text{cm}^{-3})^{-0.46}$.

(v) The feedback efficiency, i.e. a fraction of the energy retained by gas from the total energy inserted by the feedback, is estimated to be approximately 10^{-3} , with almost flat distribution according to n_{hm} .

Future transition of our model to the three dimensions will enable the inclusion of turbulence, address non-spherical instabilities, and allow star formation to take place in sites other than the centre e.g. in the compressed shell, towards an thorough insight into the processes that govern the internal properties of GMCs.

ACKNOWLEDGMENTS

M.K., R.W., J.P., and S.E. acknowledge financial support from the Czech Science foundation GAČR under grant number 19-15008S and by the Astronomical Institute of the Czech Academy of Sciences through the project RVO:67985815. M.K. has also received funding from the European Union’s Framework Programme for Research and

Innovation Horizon 2020 (2014-2020) under the Marie Skłodowska-Curie Grant Agreement No. 823734. S.M.-G. and G.T.-T. were partly supported by CONACYT-México research grant A1-S-28458. S.M.-G. also acknowledges support by CONACYT through project n.482 of the “Programa Investigadoras e Investigadores por México”.

DATA AVAILABILITY

The data underlying this article will be shared on reasonable request to the corresponding author.

REFERENCES

- Ali A. A., 2021, *MNRAS*, **501**, 4136
- Asplund M., Grevesse N., Sauval A. J., Scott P., 2009, *ARA&A*, **47**, 481
- Barnes A. T., Longmore S. N., Dale J. E., Krumholz M. R., Kruijssen J. M. D., Bigiel F., 2020, *MNRAS*, **498**, 4906
- Bending T. J. R., Dobbs C. L., Bate M. R., 2020, *MNRAS*, **495**, 1672
- Bertoldi F., McKee C. F., 1990, *ApJ*, **354**, 529
- Bertram E., Glover S. C. O., Clark P. C., Klessen R. S., 2015, *MNRAS*, **451**, 3679
- Bigiel F., Leroy A., Walter F., Brinks E., de Blok W. J. G., Madore B., Thornley M. D., 2008, *AJ*, **136**, 2846
- Bosch G., Terlevich E., Terlevich R., 2009, *AJ*, **137**, 3437
- Cantó J., Raga A. C., Rodríguez L. F., 2000, *ApJ*, **536**, 896
- Castor J., McCray R., Weaver R., 1975, *ApJ*, **200**, L107
- Chabrier G., 2003, *PASP*, **115**, 763
- Chevalier R. A., Clegg A. W., 1985, *Nature*, **317**, 44
- Chevance M., et al., 2020, *MNRAS*, **493**, 2872
- Chevance M., et al., 2022, *MNRAS*, **509**, 272
- Cignoni M., et al., 2015, *ApJ*, **811**, 76
- Clark P. C., Bonnell I. A., 2004, *MNRAS*, **347**, L36
- Colella P., Woodward P. R., 1984, *Journal of Computational Physics*, **54**, 174
- Colín P., Vázquez-Semadeni E., Gómez G. C., 2013, *MNRAS*, **435**, 1701
- Colombo D., et al., 2014, *ApJ*, **784**, 3
- Colombo D., et al., 2018, *MNRAS*, **475**, 1791
- Corbelli E., et al., 2017, *A&A*, **601**, A146
- Dale J. E., Ercolano B., Bonnell I. A., 2012, *MNRAS*, **424**, 377
- Dale J. E., Ngoumou J., Ercolano B., Bonnell I. A., 2014, *MNRAS*, **442**, 694
- De Marchi G., et al., 2011, *ApJ*, **739**, 27
- Dobbs C. L., Pringle J. E., 2013, *MNRAS*, **432**, 653
- Dobbs C. L., Burkert A., Pringle J. E., 2011, *MNRAS*, **413**, 2935
- Draine B. T., 2011, *ApJ*, **732**, 100
- Dunne B. C., Chu Y.-H., Chen C. H. R., Lowry J. D., Townsley L., Gruendl R. A., Guerrero M. A., Rosado M., 2003, *ApJ*, **590**, 306
- Elmegreen B. G., Scalo J., 2004, *ARA&A*, **42**, 211
- Espinoza P., Selman F. J., Melnick J., 2009, *A&A*, **501**, 563
- Evans Neal J. I., et al., 2009, *ApJS*, **181**, 321
- Federrath C., Klessen R. S., 2012, *ApJ*, **761**, 156
- Fryxell B., et al., 2000, *ApJS*, **131**, 273
- Fukui Y., Habe A., Inoue T., Enokiya R., Tachihara K., 2021, *PASJ*, **73**, S1
- Fukushima H., Yajima H., Sugimura K., Hosokawa T., Omukai K., Matsumoto T., 2020, *MNRAS*, **497**, 3830
- Girichidis P., Federrath C., Allison R., Banerjee R., Klessen R. S., 2012, *MNRAS*, **420**, 3264
- Grasha K., et al., 2018, *MNRAS*, **481**, 1016
- Grasha K., et al., 2019, *MNRAS*, **483**, 4707
- Grudić M. Y., Hopkins P. F., Lee E. J., Murray N., Faucher-Giguère C.-A., Johnson L. C., 2019, *MNRAS*, **488**, 1501
- Gupta S., Nath B. B., Sharma P., Shchekinov Y., 2016, *MNRAS*, **462**, 4532
- Hannon S., et al., 2019, *MNRAS*, **490**, 4648
- Hollyhead K., Bastian N., Adamo A., Silva-Villa E., Dale J., Ryon J. E., Gazak Z., 2015, *MNRAS*, **449**, 1106
- Hopkins P. F., Quataert E., Murray N., 2011, *MNRAS*, **417**, 950
- Howard C. S., Pudritz R. E., Harris W. E., 2016, *MNRAS*, **461**, 2953
- Hughes A., et al., 2013, *ApJ*, **779**, 46
- Jeffreson S. M. R., Kruijssen J. M. D., 2018, *MNRAS*, **476**, 3688
- Kim J.-G., Kim W.-T., Ostriker E. C., 2018, *ApJ*, **859**, 68
- Kim J.-G., Ostriker E. C., Filippova N., 2021, *ApJ*, **911**, 128
- King I., 1962, *AJ*, **67**, 471
- Klessen R. S., Heitsch F., Mac Low M.-M., 2000, *ApJ*, **535**, 887
- Koda J., et al., 2009, *ApJ*, **700**, L132
- Koyama H., Inutsuka S.-i., 2002, *ApJ*, **564**, L97
- Kreckel K., et al., 2018, *ApJ*, **863**, L21
- Kruijssen J. M. D., et al., 2019a, *MNRAS*, **484**, 5734
- Kruijssen J. M. D., et al., 2019b, *Nature*, **569**, 519
- Krumholz M. R., Matzner C. D., 2009, *ApJ*, **703**, 1352
- Lancaster L., Ostriker E. C., Kim J.-G., Kim C.-G., 2021, *ApJ*, **914**, 89
- Lee E. J., Chang P., Murray N., 2015, *ApJ*, **800**, 49
- Leroy A. K., et al., 2017, *ApJ*, **846**, 71
- Lucas W. E., Bonnell I. A., Dale J. E., 2020, *MNRAS*, **493**, 4700
- Mac Low M.-M., Klessen R. S., 2004, *Reviews of Modern Physics*, **76**, 125
- Martínez-González S., Silich S., Tenorio-Tagle G., 2014, *ApJ*, **785**, 164
- Maschberger T., 2013, *MNRAS*, **429**, 1725
- Massey P., Hunter D. A., 1998, *ApJ*, **493**, 180
- Matzner C. D., 2002, *ApJ*, **566**, 302
- McLeod A. F., Dale J. E., Evans C. J., Ginsburg A., Kruijssen J. M. D., Pellegrini E. W., Ramsay S. K., Testi L., 2019, *MNRAS*, **486**, 5263
- Meidt S. E., et al., 2020, *ApJ*, **892**, 73
- Menon S. H., Federrath C., Krumholz M. R., 2022, *MNRAS*, **517**, 1313
- Ninkovic S., 1998, *Serbian Astronomical Journal*, **158**, 15
- Onodera S., et al., 2010, *ApJ*, **722**, L127
- Osterbrock D. E., 1974, *Astrophysics of gaseous nebulae*. University Science Books
- Padoan P., Nordlund Å., 2011, *ApJ*, **730**, 40
- Padoan P., Haugbølle T., Nordlund Å., 2012, *ApJ*, **759**, L27
- Padoan P., Pan L., Haugbølle T., Nordlund Å., 2016, *ApJ*, **822**, 11
- Pellegrini E. W., Baldwin J. A., Ferland G. J., 2011, *ApJ*, **738**, 34
- Rahner D., Pellegrini E. W., Glover S. C. O., Klessen R. S., 2017, *MNRAS*, **470**, 4453
- Rahner D., Pellegrini E. W., Glover S. C. O., Klessen R. S., 2018, *MNRAS*, **473**, L11
- Raskutti S., Ostriker E. C., Skinner M. A., 2016, *ApJ*, **829**, 130
- Raskutti S., Ostriker E. C., Skinner M. A., 2017, *ApJ*, **850**, 112
- Rey-Raposo R., Dobbs C., Agertz O., Alig C., 2017, *MNRAS*, **464**, 3536
- Rogers H., Pittard J. M., 2013, *MNRAS*, **431**, 1337
- Rugel M. R., et al., 2019, *A&A*, **622**, A48
- Sabbi E., et al., 2012, *ApJ*, **754**, L37
- Schure K. M., Kosenko D., Kaastra J. S., Keppens R., Vink J., 2009, *A&A*, **508**, 751
- Scoville N. Z., Hersh K., 1979, *ApJ*, **229**, 578
- Selman F., Melnick J., Bosch G., Terlevich R., 1999, *A&A*, **347**, 532
- Semenov V. A., Kravtsov A. V., Gnedin N. Y., 2016, *ApJ*, **826**, 200
- Semenov V. A., Kravtsov A. V., Gnedin N. Y., 2021, *ApJ*, **918**, 13
- Shetty R., Beaumont C. N., Burton M. G., Kelly B. C., Klessen R. S., 2012, *MNRAS*, **425**, 720
- Silich S., Tenorio-Tagle G., 2013, *ApJ*, **765**, 43
- Silich S., Tenorio-Tagle G., Rodríguez-González A., 2004, *ApJ*, **610**, 226
- Skinner M. A., Ostriker E. C., 2015, *ApJ*, **809**, 187
- Sun J., et al., 2020, *ApJ*, **901**, L8
- Szécsi D., Agrawal P., Wünsch R., Langer N., 2022, *A&A*, **658**, A125
- Tenorio-Tagle G., 1979, *A&A*, **71**, 59
- Tenorio-Tagle G., Palouš J., Silich S., Medina-Tanco G. A., Muñoz-Tuñón C., 2003, *A&A*, **411**, 397
- Tenorio-Tagle G., Wünsch R., Silich S., Palouš J., 2007, *ApJ*, **658**, 1196
- Turner J. A., et al., 2022, *MNRAS*, **516**, 4612
- Utomo D., et al., 2018, *ApJ*, **861**, L18
- Vutisalchavakul N., Evans Neal J. I., Heyer M., 2016, *ApJ*, **831**, 73
- Walch S. K., Whitworth A. P., Bisbas T., Wünsch R., Hubber D., 2012, *MNRAS*, **427**, 625
- Walch S., et al., 2015, *MNRAS*, **454**, 238
- Weaver R., McCray R., Castor J., Shapiro P., Moore R., 1977, *ApJ*, **218**, 377
- Wei L. H., Keto E., Ho L. C., 2012, *ApJ*, **750**, 136

Whitworth A., 1979, [MNRAS](#), **186**, 59

Wong T., et al., 2011, [ApJS](#), **197**, 16

Wünsch R., Tenorio-Tagle G., Palouš J., Silich S., 2008, [ApJ](#), **683**, 683

Wünsch R., Palouš J., Tenorio-Tagle G., Ehlerová S., 2017, [ApJ](#), **835**, 60

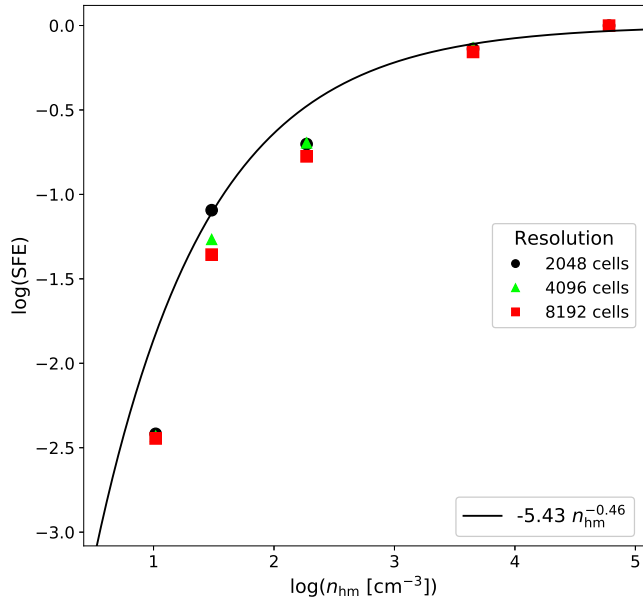


Figure A1. Same as in Fig. 7, for five cloud models under setup B, which were tested under three refinement levels (see text). For reference, we display the fit curve to the entire set of setup B models (Eq. 24).

APPENDIX A: DEPENDENCE ON RESOLUTION

We explore the effect that the grid resolution has on our results. We run setup B simulations with five sets of input parameters for the cloud mass, radius, and density slope; $(M_{\text{cld}}, R_{\text{cld}}, \beta) = (10^{4.5} M_{\odot}, 20 \text{ pc}, 1.4), (10^{4.5} M_{\odot}, 30 \text{ pc}, 0.8), (10^{4.5} M_{\odot}, 20 \text{ pc}, 1.2), (10^{5.5} M_{\odot}, 20 \text{ pc}, 1.6),$ and $(10^6 M_{\odot}, 10 \text{ pc}, 1.8)$. For our test purposes, the computational domain was divided into 2048, 4096, and 8192 grid cells. Following our description in §4.3, we calculated the half-mass densities of the model clouds and display them against the resulting SFEs in Fig. A1, similar as in Fig. 7. For a given cloud model, the discrepancy in the SFEs due to the different resolutions is shown to be, in general, within ~ 0.1 dex.

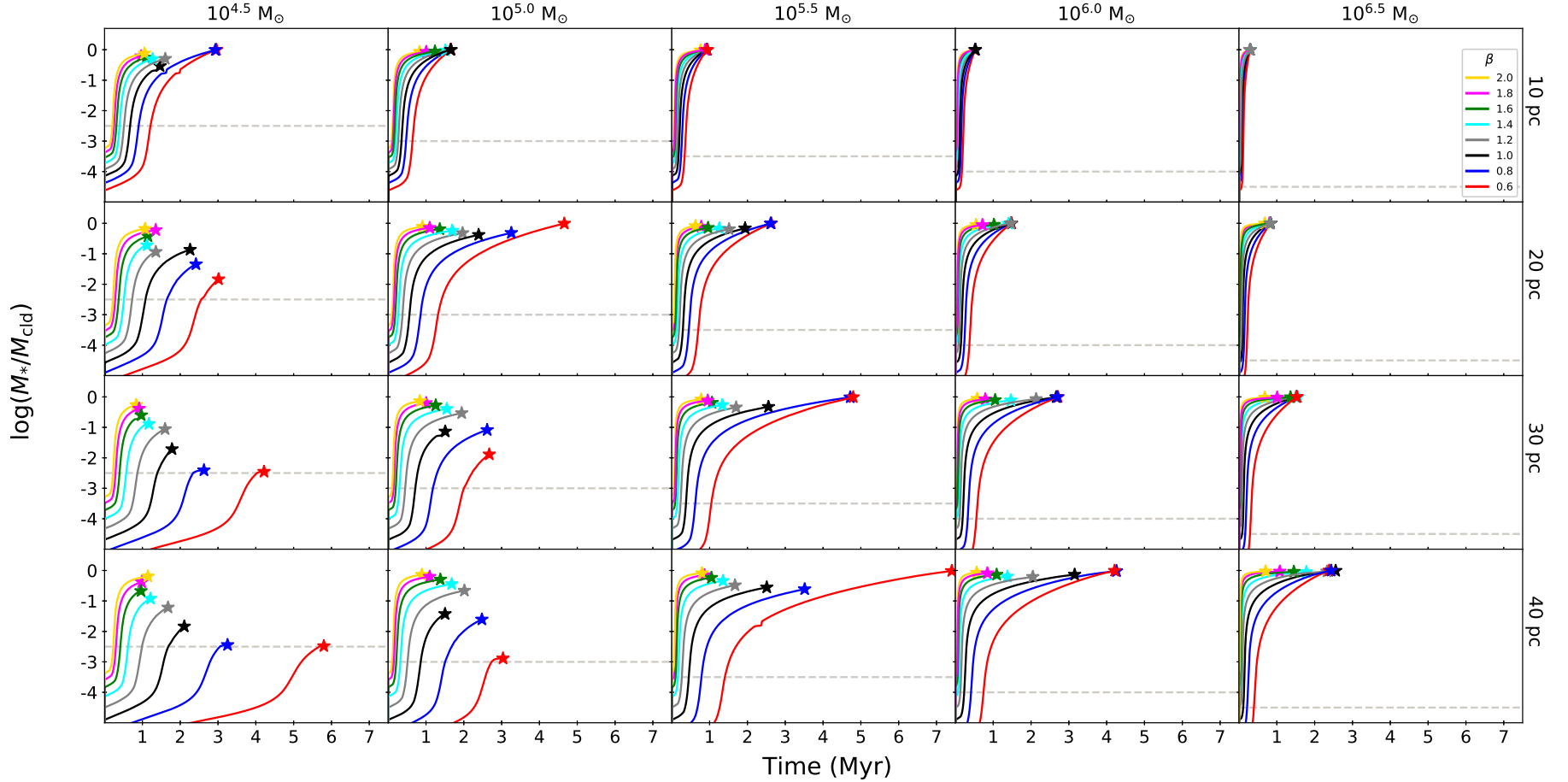


Figure B1. Same as in Fig. 6, for the different cloud models of the explored parameter space. The calculations on the growth of the stellar mass are color coded with respect to the steepness β of the density profile, with designations given in the upper right panel.

APPENDIX B: SETUP B RUNS - ENTIRE SET

Calculations over the entire set of cloud parameters are displayed in Fig. B1, showing the dependence of SFE on M_{cld} and R_{cld} . Generally, SFE is lower for lower M_{cld} and higher R_{cld} . These relations are valid both when comparing models with other parameters fixed, and also for $\text{SFE}(\beta_{\text{min}})$. This is expected, because more strongly gravitationally bound clouds need more feedback energy and hence higher mass star cluster to be disrupted. Additionally, β_{min} gets higher for higher M_{cld} and lower R_{cld} . Note that, the lowest measured SFE in models with $M_{\text{cld}} = 10^{4.5} - 10^{5.0} M_{\odot}$ and $R_{\text{cld}} = 30 - 40$ pc is constrained by the threshold mass of the cluster for initiating feedback, M_{SF} (dashed line).